

Article

Synthetic Aperture Radar Doppler Tomography Reveals Details of Undiscovered High-Resolution Internal Structure of the Great Pyramid of Giza

Filippo Biondi ^{1,†,‡} and Corrado Malanga ^{2,*,‡}

¹ Department of Electronic and Electrical Engineering, University of Strathclyde, Glasgow G1 1XW, UK

² Department of Chemistry and Industrial Chemistry, University of Pisa, Via Giuseppe Moruzzi 13, 56100 Pisa, Italy

* Correspondence: corrado.malanga@unipi.it; Tel.: +39-342-723-7507

† Current address: Via Perella 36, 06073 Corciano, Italy.

‡ These authors contributed equally to this work.

Abstract: A problem with synthetic aperture radar (SAR) is that due to the poor penetrating action of electromagnetic waves inside solid bodies, the capability to observe inside distributed targets is precluded. Under these conditions, imaging action is provided only on the surface of distributed targets. The present work describes an imaging method based on the analysis of micro-movements on the Khnum-Khufu Pyramid, which are usually generated by background seismic waves. The obtained results prove to be very promising, as high-resolution full 3D tomographic imaging of the pyramid's interior and subsurface was achieved. Khnum-Khufu becomes transparent when observed in the micro-movement domain. Based on this novelty, we have completely reconstructed internal objects, observing and measuring structures that have never been discovered before. The experimental results are estimated by processing series of SAR images from the second-generation Italian COSMO-SkyMed satellite system, demonstrating the effectiveness of the proposed method.

Keywords: synthetic aperture radar; doppler frequencies; multi-chromatic analysis; micro motion; pyramid of Khnum-Khufu; sonic images



Citation: Biondi, F.; Malanga, C. Synthetic Aperture Radar Doppler Tomography Reveals Details of Undiscovered High-Resolution Internal Structure of the Great Pyramid of Giza. *Remote Sens.* **2022**, *14*, 5231. <https://doi.org/10.3390/rs14205231>

Academic Editors: Rosa Lasaponara, Ilaria Catapano, Luca Piroddi, Sebastiano D'Amico, Marilena Cozzolino, Nasser Abu Zeid, Patrizia Capizzi and Sergio Vincenzo Calcina

Received: 30 August 2022

Accepted: 12 October 2022

Published: 19 October 2022

Publisher's Note: MDPI stays neutral with regard to jurisdictional claims in published maps and institutional affiliations.



Copyright: © 2022 by the authors. Licensee MDPI, Basel, Switzerland. This article is an open access article distributed under the terms and conditions of the Creative Commons Attribution (CC BY) license (<https://creativecommons.org/licenses/by/4.0/>).

1. Introduction

The Pyramid of Khnum-Khufu, also known as the Great Pyramid of Giza or Cheops, is the oldest and largest of the three main pyramids that are part of the necropolis of Giza (Egypt). The infrastructure is built with blocks of granite, weighing approximately 2.5 t each. Completion of the work is estimated to have taken at least two and a half million blocks, put in place with millimeter precision in a short period of time, estimated at around 15 or 30 years [1]. Despite being one of the oldest and largest monuments on Earth, to date, there is still no common and scientifically established idea on how the pyramids of Egypt were built [2,3]. The Red Sea was the most important Harbor Facilities at the time of King Khufu [4], where an exceptionally well-preserved harbor complex from the Early Old Kingdom at Wadi al-Jarf along the Egyptian coast of the Red Sea has been excavated.

1.1. Egyptology Engineering and Ultrasound Introduction

In studying the origin of the pyramids, we believe we should not overlook the existence of ancient mythological writings. A study concerning the myths and folklore of the ancient peoples of the world, highlighting all the similarities between them, was made in [5]. The argument that myths are insignificant—often considered mere stories passed on through generations—has been challenged. The authors are open to the possibility that a technologically more advanced civilization existed before a known timeline, where the existence of various glacial ages [6] prevented the passing down of history. They focus on

the mythical cities mentioned in ancient Indian texts, describing how that subcontinent was an integral part of this [7,8]. However, how the Egyptian Pyramids were built has remained an enduring mystery [9–11]. A theory that the pyramids were cast of cement-like conglomerate made directly *in situ* using granular limestone aggregates and an alkali–silicate binder is proposed in [12], and evidence is also discussed in [13,14]. In order to obtain an accurate perception of how the pyramids were constructed, various engineering hypotheses were evaluated in [15], noting that in their current form, they lay the foundations for new theories. At present, the general academic consensus is that pyramids served as funerary monuments and burial sites for the pharaohs. However, it is also widely theorized that such infrastructures may have been built for another purpose. On an aseptic panoramic view, many connections can be found between the pyramids, vibrations and many mechanical devices reminiscent of hydraulic systems, resonance chambers and acoustic filters [16,17]. The energy to make the pyramids vibrate can be provided by the natural environment, and the Earth’s atmosphere infrasound vibrations may provide the source of such energy [18]. This provides a basis for the discussion of special classes of waves, including mountain Lee-waves, infrasound, progressive waves in the lower atmosphere, and waves in the upper atmosphere and ionosphere [19]. Atmospheric sound models extended to the combination effects of both finite depth ocean and source directivity in both elevation and azimuth angles are studied in [20].

Acoustic waves are widely used in the field of archaeology. The acoustics of three important World Heritage sites such as the five caves in Spain, the Stonehenge stone circle in England and the Paphos Theatre in Cyprus are studied in [21]. Groundwater can influence the geomagnetic field measured in the subsurface. The level of water in the rock determines its electrical conductivity and thus changes the magnitude of the telluric currents induced in the rock by the change in magnetic fields generated in the ionosphere. This can be studied by using several magnetometers at different points in the subsurface. Geomagnetic signals using two magnetometers were successfully monitored in [22] by setting an optimal electrokinetic magnitude signal upper-bound. A methodology used for self-potential and seismic–electromagnetic measurements, both for on-site and laboratory experiments as well as for modeling, is extensively described in [23]. The research also provides the bibliography on studies carried out in hydrology to remotely detect water flows, to deduce their thickness, and to predict their hydraulic conductivity. The observation method discussed also proposes the detection of fractures in wells, which is also useful in trying to study earthquakes. Recent theoretical and experimental studies have produced several unusual and interesting results on the cold fusion of matter experienced on dense lithium [24]. The existence of this exciting property of matter relates to zero-point energy estimates that suggest quantum effects play a significant role in shaping the phase diagram of lithium. The vibration-induced property change in the melting and solidifying process of silver nanoparticles with the use of molecular dynamics simulation was found in [25].

The general problem of acoustic wave propagation through parallel paths is addressed by the information theory of two-port telecommunication networks. This allows any mechanical system to be considered as a single element with two gates. Such a circuit is schematically represented with concentrated elements by admittance that have a value compared to the sum of the corresponding instantaneous admittance existing along the parallel paths. In order to calculate all parameters including those representing transmission losses (e.g., the standing wave ratio), in the case of a non-adaptive paths, the theory of transmission lines is well applicable. A Quincke tube acoustic filter therefore uses two parallel paths. In order to optimize the maximum wave propagation through the system, the Quincke tube must be adapted and, through the choice of length and thickness of the ducts, can produce a selective transmission loss, so that it can operate as an acoustic filter. In [26], the transmission loss characteristics of several other variations in duct sizes and lengths are presented together with some very limited experimental data. The phenomenon of pressure pulsations in pipeline systems caused by centrifugal pumps or reciprocating compressors is known to have detrimental effects on industrial applications. An experi-

mental investigation of the attenuation mechanism of a Herschel–Quincke device and its effectiveness in damping pressure pulsations when applied to a resonant piping system had been presented in [27].

The development of mechanical engineering in ancient Egypt through the stone industry was described in [28], covering the period from the Predynastic to the Old Kingdom. The characteristics and innovations of stone vessels available in these periods were analyzed. Conventional sound absorbers can hardly possess the good performance of low-frequency and broadband absorption simultaneously. In order to combine these two functions into one kind of absorbers, the gradually perforated porous materials backed with Helmholtz resonant cavity are proposed in [29]. A strategy to design three-dimensional elastic periodic structures endowed with complete band-gaps, the first of which is ultra-wide, where the top limits of the first two band-gaps are overstepped in terms of wave transmission in the finite structure is proposed in [30]. Thus, subsequent band-gaps are merged, approaching the behavior of a three-dimensional low-pass mechanical filter.

The debate on how the granite blocks could have been transported up the full height of the pyramids is still an open one. To this end, the theory of in situ formation of the blocks by means of a cement mixture has also been formulated. Most synthetic stones can be made from re-agglomerated materials. Starting with a mineral substance such as granite rock or naturally eroded, disintegrated or not-aggregated limestone, it is given a compact structure using a binder, such as a geological glue that agglomerates to bond the mineral particles to each other. The result is a new rock with the same mechanical characteristics as a natural equivalent. Such a technique is supposed to have been used to build the pyramid of Khnum-Khufu [12,31].

1.2. Archaeology Heritage Investigation Introduction

Back to the pyramid of Khnum-Khufu, for over a century, it has been known that the beams forming the ceiling of the King's Chamber and those of the first and second Relieving Chambers in the Great Pyramid are cracked. However, the temporal origin of these cracks is still unknown. The results of a 3D virtual reality computer simulation designed to determine precisely when the beams cracked are reported in [32]. Several 3D imaging techniques applied on the Khnum-Khufu pyramid are developed in [33]. Among all the theories formulated to try to explain how the pyramid of Khnum-Khufu was built, there is also the hypothesis of the existence of an internal ramp that goes around the pyramid several times. This theory could prove the fact that the pyramid could have been built in twenty years [34]. Microgravity surveys of the Khnum-Khufu pyramid have been conducted, considering also the general structure of the pyramid. A new interpretation technique for the endoscopy of large finite bodies has been developed in [35]. In order to carry out non-invasive internal scans of the pyramid [36], using electromagnetic waves, it is necessary to use special georadar [37], which however has the limitation of having little penetration inside the granite.

The study of ancient Egyptian monuments attracted the attention of experts all over the world. A recent event that confirms this is the discovery, using muon sensors [38,39], of the presence of a previously unknown cavity located inside the pyramid of Khnum-Khufu. Since this discovery cannot be directly confirmed by drilling, another independent non-destructive method is needed to confirm this discovery and provide an accurate determination of the location and shape of the cavity. A possible holographic radar simulation framework for the detection of openings or other unknown structures of interest is analyzed in [36]. Research [40] for the first time investigated the possibility of using cosmic-ray detectors involved their ability to measure the angle of arrival of penetrating cosmic rays muons with great precision over a large sensitive area. In [41], the authors reported the discovery of a large void (with a cross-section similar to that of the Grand Gallery and a minimum length of 30 m) situated above the Grand Gallery.

The investigation of the microgravimetric measurements on the side of a pyramid could also map the recently discovered “muon chamber” in the Great Pyramid of Khnum-

Khufu in Egypt. In [42], the exploitation of technical capabilities of modern gravimeters is used to perform three-dimensional model calculations with realistic model parameters. A gradiometer survey has been carried out in [43] over a surface area of $100\text{ m} \times 100\text{ m}$ to achieve the purpose, and the magnetic data were processed using Geoplot software in order to obtain high-quality images of hidden structures inside the Khnum-Khufu pyramid. The results obtained show the presence of interconnected large tomb structures composed of mud-bricks; some other ancient rooms and walls are also present.

A climbing robot called “Djedi” has been designed, constructed, and deployed in [44] to explore shafts of the Queen’s chamber within the Great Pyramid. The Djedi robot is based on the concept of inchworm motion and is capable of carrying a long reach drill or snake camera. The robot successfully climbed the southern shaft of the Great Pyramid, deployed its snake camera, and revealed writing not seen for thousands of years. Robot design, including climbing steps in the shaft and lessons learned from experimental deployment, has been designed in [44].

1.3. Synthetic Aperture Radar Introduction

Satellite remote sensing is widely used in the field of archaeology [45,46]. Data from the use of SAR to survey the southern Maya plains suggest that large areas were continuously drained by ancient canals that may have been used for intensive cultivation. In agreement with the authors of [47], SAR remote sensing confirmed the existence of the canals. Through excavations and in situ ground surveys, they provided sufficient comparative information. Correlating all the data, it was concluded that the Maya civilization, of the Late Classic period, was firmly based on the intensive and large-scale cultivation of marshy areas. Research [48] found an ideal model configuration, associated with spiral ramps, demonstrating how Egyptians could have built the pyramids. In the past, Synthetic Aperture Radar (SAR) vibrations have been very useful in estimating key vessel characteristics. Research [49,50] proposed a novel strategy to estimate the micro-motion (MM) of ships from SAR images. The proposed approach is for the MM estimation of ships, occupying thousands of pixels, which processes the information generated during the coregistration of several re-synthesized time-domain and not overlapped Doppler sub-apertures of the COSMO-SkyMed satellite single-look complex (SLC) data. The multi-chromatic analysis (MCA), coined for the first time in [51], and performed in the range direction, allows retrieving unambiguous height information on selected pixels, potentially solving the problem of spatial phase unwrapping and absolute phase measurement of interferometric SAR data, under the condition of a sufficient Chirp bandwidth present on both coregistered master and slave SAR SLC images. The authors of [52] propose a new procedure to monitor critical infrastructures such as the Mosul dam, processing COSMO-SkyMed data. The proposed procedure is an in-depth modal assessment based on the MM estimation through a Doppler sub-apertures tracking and the innovation of 90° tilted Doppler-domain MCA. The procedure described above was made available to perform a comprehensive survey of large road bridges, according to [53]. The authors of [52,54,55] successfully formulated a comprehensive procedure to perform structural health monitoring using SAR. The technique allows one to successfully estimate the position and shape of cracks on bridges in order to prevent their collapse. The method is based initially on the persistent scatterers interferometry [56,57] that is also discussed for completeness and validation. The modal analysis has detected the presence of several areas of resonance that could mean the presence of cracks, and the results have shown that the dam is still in a strong destabilization. The article provides an in-depth study of the physical characteristics of vibrations in terms of amplitude, frequency, polarization, and robustness of the estimate in terms of the signal-to-noise ratio of each SAR pixel considered, both through the evaluation of simulated data and by processing real data.

In this paper, we use a new method based on the tomographic reconstruction of MM, with the aim of performing imaging of the principal targets that make the main internal structure of the pyramid visible. We use the similar methods already experimented in [58]

to search for cracks in large infrastructures but not for tomography. The physical principle we use is that of estimating the vibrations captured by the Khnum-Khufu pyramid during the SAR observation time interval. The vibration estimation is completed by evaluating the Doppler centroid anomalies, which is an indispensable parameter that is used during the SAR azimuth focusing process. We use Doppler sub-apertures to estimate the vibrations present on the pyramid. The vibration energy is generated from many sources such as wind. Great contribution in terms of vibration energy is also generated by the city of Cairo, which is located closely to the pyramid of Khnum-Khufu and by the presence of the Nile river.

Given the large number of articles belonging to the previous literature, which has been conducted in the field of SAR, it is necessary to consider the following works: when the ‘stop-and-go approximation’, during the azimuth SAR focusing process, is no longer valid, it occurs that in addition to the constant Doppler frequency shift induced by the satellite’s movement along its orbit, the target under consideration is subjected to micro-movement dynamics, such as mechanical vibrations or rotations. Such movements and accelerations, generated by the micro-movement dynamics, induce the micro-Doppler effect, which is directly attributable to various defocusing and spatial delocalization effects [59]. However, all those phenomena that generate artefacts from SAR image formation can represent an information resource. In fact, we exploit the artefact that is produced when a vibrating target is observed. The authors of [60] present an experimentally validated model that provides accurate localization and the shape of coupled echoes of vibrating targets in both near-field and far-field SAR images.

The successful experimental realization of polarimetric airborne SAR tomography is demonstrated for the first time in [61]. The authors present the concept of aperture synthesis for tomographic imaging for the case of a multi-baseline imaging geometry and discuss the constraints arising from the limited number of flight tracks. Superficial targets profiles detection and tomographic imaging connected to the electromagnetic penetration capabilities is achieved. This propriety depends on the used wavelengths, which is usually poor. The effects of phase miscalibration due to residual uncompensated atmospheric contribution and temporal SAR phase decorrelation is analyzed in [62]. The tomographic potential of high-resolution satellite images such as TerraSAR-X spotlight data of an urban environment is demonstrated in [63].

Biondi [49] proposed a new approach concerning the MM estimation of ships, processing the information given by sub-pixel tracking generated during the coregistration process of two re-synthesized time-domain and partially overlapped Doppler sub-apertures generated by splitting the raw data observed by a single wide azimuth band SAR image. Additionally, the predominant vibrational modes of different ships are then estimated in [50]. The performance analysis is conducted on one spotlight SAR image recorded by the COSMO-SkyMed satellite system, paving the way for application to the surveillance of land-based industry activities. A complete procedure for damage early-warning detection, by using MM estimation of critical sites, based on modal proprieties analysis has been assessed in [54]. Particularly, MM is processed to extract modal features such as natural frequencies and mode shapes generated by vibrations of large infrastructures. Problems connected to SAR acquisitions are that due to the poor penetrating action of electromagnetic waves within solid bodies, the ability to see through distributed targets is precluded. An imaging method based on the analysis of MMs present in volcanoes and generated by the Earth’s underground seismic energy is described in [64], using penetrating tomographic imaging over a depth of about 3 km from the Earth’s surface. The work describes also a complete assessment focused on showing the perfect space–time-frequency synchronization of SAR estimated vibrations with respect to seismic ripple estimated through in situ earthquake instruments.

Considering the experience gathered in the field of mechanical vibration estimation using radar, taking into account the imaging results addressed within volcanoes, considering all the calibration, validation as well as performance estimation experiments extensively described in [49,50,52,54], we processed several SAR images observed in the Vertical–Vertical

(VV) polarization, and the estimated MM allows us to visualize the principal internal components present in the pyramid.

We can state that the experimental results we propose definitively solve one of the oldest mysteries of human existence, the complete solution of the internal structure of Khnum-Khufu. To this end, in order to provide a more complete contribution to our work, we have firstly investigated the details of the external structure of all the pyramids belonging to the Giza Plateau (Khufu, Kefren and Menkaure); then, we concentrated on studying the internal structure of the pyramid of Khnum-Khufu alone, providing a complete and detailed 3D reconstruction of all the known and unknown chambers, based on tomographic SAR measurements. In the paper, we provide a complete list of the internal structures measured by tomography, each of them marked with a unique sequential number.

Table 1 lists the principal characteristics of the radar we used for the experiments.

Table 1. Principal parameters of the SAR acquisitions.

SAR Parameter	Value
Central frequency	9.6 GHz
Chirp bandwidth	400 MHz
Doppler bandwidth	22 kHz
PRF	2.0 kHz
PRT	0.23 ms
Antenna length	6 m
Type of acquisition	Spotlight
Polarization	HH, VV
Acquisition duration	15 s
Platform velocity	7 km/s
Observation height	650,000 m

2. Giza Plateau Presentation and Description

The pyramid of Khnum-Khufu is a monumental structure built mainly of granite blocks; its orientation is almost perfectly aligned to the north. The monumental complex of the Giza plateau is represented in Figure 1. The three pyramids, Khnum-Khufu (top right), Kefren (located in the center) and Menkaure (the last on the bottom left) can be observed. In this context, our work focuses on visualizing the vibrational tomographic profile of the pyramid of Khnum-Khufu. Figure 2a is the schematic representation of the north–south central section of the infrastructure. The figure represents the schematic of what is known, and the main parts of the infrastructure are numbered sequentially from 1 to 11. The object consists of the Zed and the King’s chamber, with its sarcophagus inside. The Zed, the details of which can be seen in Figure 2b,c, is a large monument made entirely of granite, consisting of an upper roof made of two oblique granite slabs, and five parallel stone slabs, spaced at varying distances from each other. Each stone has its upper face not smooth, so each surface has a pronounced roughness. On the contrary, each of its lower faces is extremely smooth. Below this monument is the King’s room. Both the Zed and the King’s room are off-axis with respect to the apex of the pyramid and are located toward the south on the north–south symmetry plane. Object 2 of Figure 2a, is the Queen’s room, a smaller volume object located on the axis of the pyramid and below the King’s room. As can be seen from Figure 2a, Object 2, unlike the King’s room, is located exactly under the apex of the pyramid. The last room is Object 3, which is also off-axis of the pyramid; it is also shifted to the south, but in this case, it is located underground. It is usually called the unfinished room. Object 4 represents a large corridor that connects the King’s room with the Queen’s room; it is called the Grand Gallery. Objects 5 and 6 are air ducts, while the remaining ducts 8, 9, and 10 connect the Grand Gallery with the Queen’s room and the unfinished room (the one located below ground). Object 7 is the entrance to the pyramid, and finally, line 11 indicates the surface on which the pyramid sits.

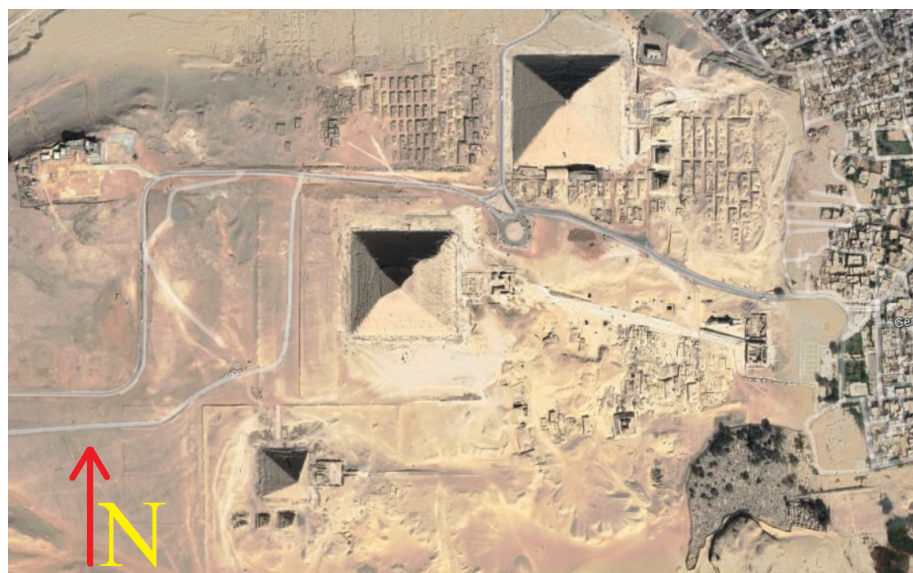


Figure 1. Optical satellite image of the Giza plateau. All pyramids are oriented to the North.

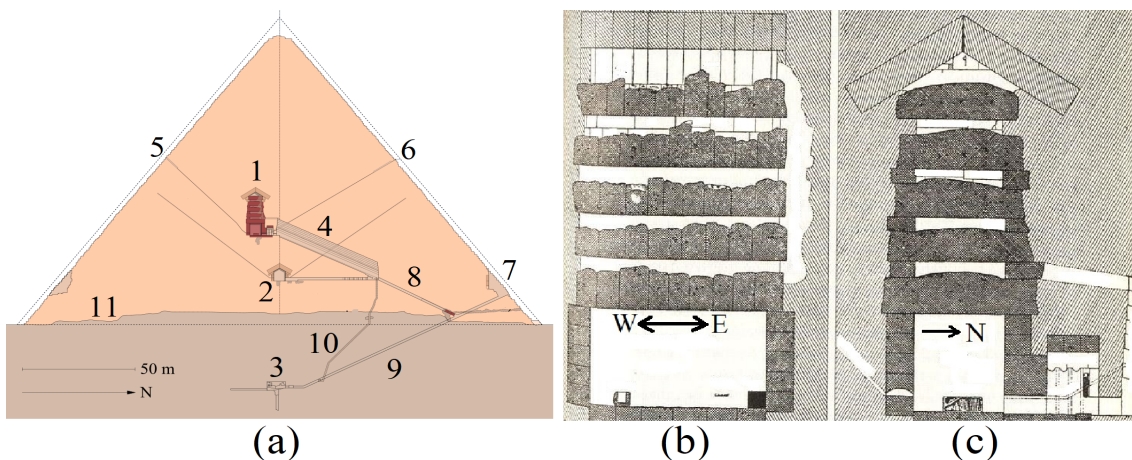


Figure 2. Khnum-Khufu diagram of the known interior structures. (a): East-side schematic view. (b): South-side view of the ZED. (c): East-side view of the ZED.

3. Methodology

In this work, the MM technique is used to perform sonic imaging by processing a single SAR image in the single-look-complex (SLC) configuration. The technique involves the MM estimation belonging to the Khnum-Khufu pyramid and is generated by the background ripple underground seismic activity that reflects superficial vibrations. The MM estimation is completed through MCA and performed in the Doppler direction. Multiple Doppler sub-apertures, SAR images with lower azimuth resolution, are generated to estimate the vibrational trend of some pixels of interest. The infra-chromatic displacement generated by Doppler centroid anomalies due to target motion and acceleration [65,66] is calculated through the pixel tracking technique, using high-performance sub-pixel coregistration [49, 50, 52, 54, 64].

In Figure 3b, we present the SAR image of the pyramid. In order to show the temporal trend vibration, we examined a pixel located within the yellow circle 1. Figures 4–6 represent the time-domain displacement in magnitude, range and azimuth, respectively. The blue plot is the unfiltered temporal displacement trend, while the red function represents its positive envelope.

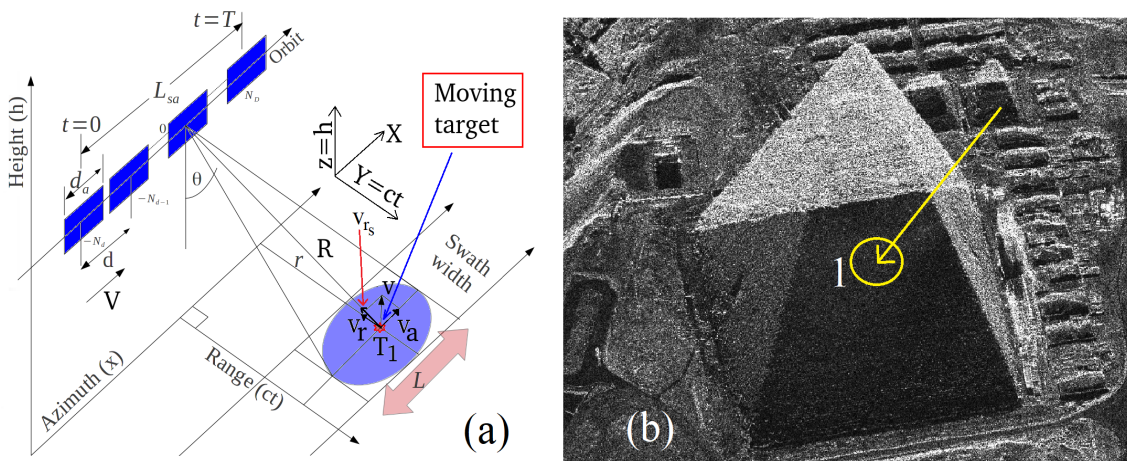


Figure 3. (a): SAR acquisition geometry. (b): SAR image in magnitude.

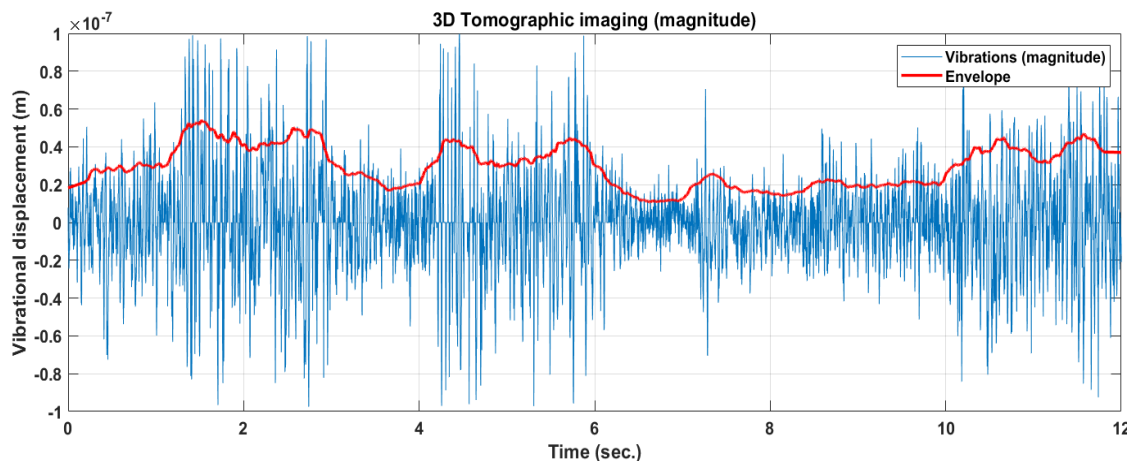


Figure 4. Time domain vibrations (magnitude).

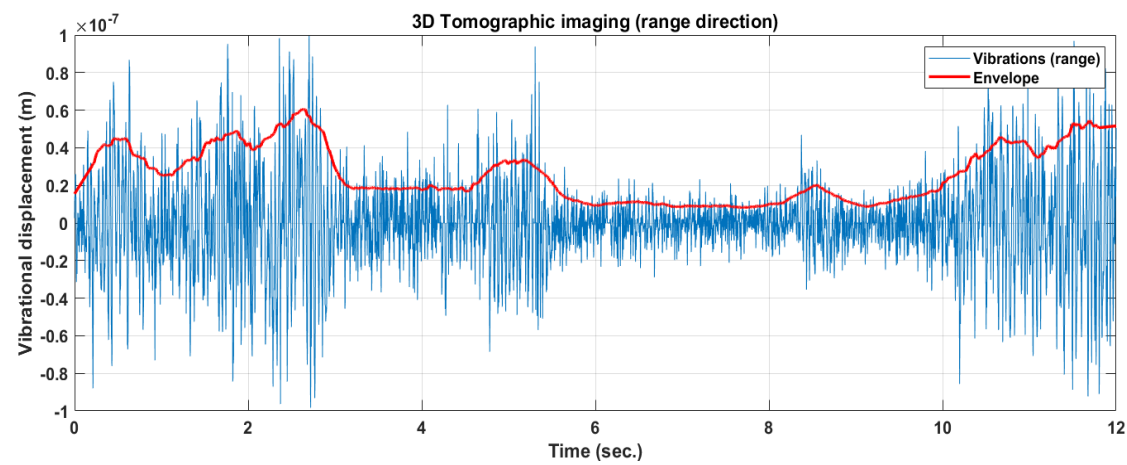


Figure 5. Time domain vibrations in the range direction (magnitude).

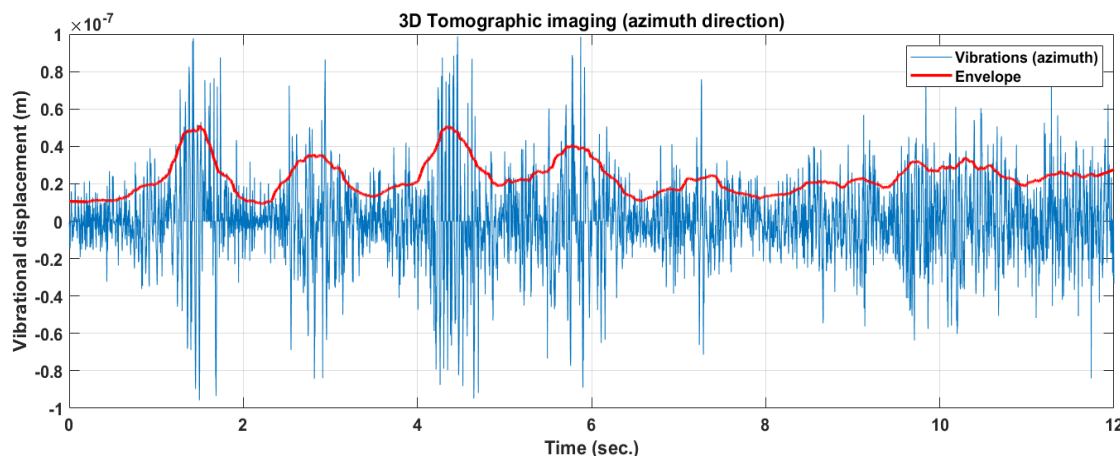


Figure 6. Time domain vibrations in the azimuth direction (magnitude).

Vibrations observed along the tomographic view direction, embedded into the multi-chromatic Doppler diversity, are focused along the height (or depth) dimension, developing metric resolution tomographic underground imaging.

The SAR synthesizes the electromagnetic image through a “side looking” acquisition, according to the observation geometry shown in Figure 3a, where:

- r is the zero-Doppler distance (constant);
- R is the slant-range;
- R_0 is the reference range at $t = 0$;
- d_a is the physical antenna aperture length;
- V is the platform velocity;
- d is the distance between two range acquisitions;
- L_{sa} is the total synthetic aperture length;
- t is the acquisition time variable;
- T is the observation duration;
- $t = 0$ and $t = T$ are the start and stop time acquisition, respectively;
- $L = \frac{\lambda r}{d_a}$ is the azimuth electromagnetic footprint width;
- θ is the incidence angle of the electromagnetic radiation pattern.

All the above parameters are related to the staring-spotlight SAR acquisition that is adopted in this work. The SAR data belonging to the electromagnetic image are formed through the focusing process that involves the application of a two-dimensional matched filter acting in the range direction and in the azimuth direction. The SLC signal resulting from compression is given by [67]:

$$s_{SLC}(k, x) = 2N\tau \exp\left[-j\frac{4\pi}{\lambda}r\right] \text{sinc}\left[\pi B_{cr}\left(k - \frac{2R}{c}\right)\right] \text{sinc}[\pi B_{cd}x] \quad (1)$$

for $x = kt$, $k = \{0, 1, \dots, N-1\}$, $x = \{0, 1, \dots, M-1\}$, with $N, M \in \mathbb{N}$.

The focused SAR signal generated by the back-scattered electromagnetic energy of a point target supposed to be stationary is represented in (1). The terms B_{cr} and $B_{cd} = \frac{4Nd}{\lambda r}$ are the total chirp and Doppler bandwidths respectively. The total synthetic aperture is equal to $L_{sa} = 2Nd$ and the azimuth resolution $\delta_D \approx \frac{1}{B_{cd}} = \frac{\lambda R}{2L_{sa}}$. In (1) the $\frac{2R}{c}$ term identifies the position in range where the maximum of the sinc function is located, while in azimuth it is centered around “zero”. In the case where the peak of the sinc function has a nonzero coordinate along the azimuth dimension, Equation (1) can be recast as:

$$s_{SLC}(k, x) = 2N\tau \exp\left[-j\frac{4\pi}{\lambda}r\right] \text{sinc}\left[\pi B_{cr}\left(k - L_{cg}\right)\right] \text{sinc}[\pi B_{cd}(x - L_{Dh})] \quad (2)$$

for $L_{cg}, L_{Dh} \in \mathbb{N}$,

where the DFT is equal to:

$$\begin{aligned}
 S_{SLC_F}(n, q) &= DFT2 \left\{ 2N\tau \exp \left[-j \frac{4\pi r}{\lambda} \right] \text{sinc} \left[\pi B_{c_r} (k - L_{c_g}) \right] \text{sinc} \left[\pi B_{c_D} (x - L_{D_h}) \right] \right\} \\
 &= 2N\tau \exp \left[-j \frac{4\pi r}{\lambda} \right] \sum_{k=0}^{N-1} \sum_{x=0}^{M-1} \text{sinc} \left[\pi B_{c_r} (k - L_{c_g}) \right] \text{sinc} \left[\pi B_{c_D} (x - L_{D_h}) \right] \\
 &\quad \exp \left(-j \frac{2\pi kn}{N} \right) \exp \left(-j \frac{2\pi xq}{M} \right) \\
 &= 2N\tau \exp \left[-j \frac{4\pi r}{\lambda} \right] \frac{1}{\pi B_{c_r}} \text{rect} \left[\frac{n}{\pi B_{c_r}} \right] \frac{1}{\pi B_{c_D}} \text{rect} \left[\frac{q}{\pi B_{c_D}} \right] \\
 &\quad \exp \left(-j 2\pi n L_{c_g} \right) \exp \left(-j 2\pi q L_{D_h} \right),
 \end{aligned} \tag{3}$$

which has a rectangular shape.

3.1. Doppler Sub-Apertures Model

In this paper, we experiment a strategy that employs Doppler sub-apertures, which are generated to measure target motion. Figure 7 represents the used bandwidth allocation strategy. From the single SAR image, we calculate the 2D digital Fourier transform (DFT) which, according to (3), has a rectangular shape. As can be seen from Figure 7, B_{c_D} is the total Doppler band synthesized with the SAR observation, while $B_{D_L} = \frac{B_{c_D}}{2}$ is the bandwidth we left out from the matched-filter boundaries to obtain a sufficient sensitivity to estimate target motions. In this context, formula (3) is the focused SAR spectrum, at maximum resolution, thus exploiting the whole band $\{B_{c_r}, B_{c_D}\}$; in accordance with the frequency allocation strategy shown in Figure 7, the following range-Doppler sub-apertures large matrix is constructed for the master multi-dimensional information:

$$S_{SLC}(k, x)_M = \begin{bmatrix} S_{SLC}(k, x)_{M_{\{1,1\}}} & S_{SLC}(k, x)_{M_{\{1,2\}}} & S_{SLC}(k, x)_{M_{\{1,3\}}} & \dots & S_{SLC}(k, x)_{M_{\{1,N_D\}}} \end{bmatrix} \tag{4}$$

for $N_D \in \mathbb{N}$,

and for the slave, the following large matrix is presented:

$$S_{SLC}(k, x)_S = \begin{bmatrix} S_{SLC}(k, x)_{S_{\{1,1\}}} & S_{SLC}(k, x)_{S_{\{1,2\}}} & S_{SLC}(k, x)_{S_{\{1,3\}}} & \dots & S_{SLC}(k, x)_{S_{\{1,N_D\}}} \end{bmatrix} \tag{5}$$

for $N_D \in \mathbb{N}$.

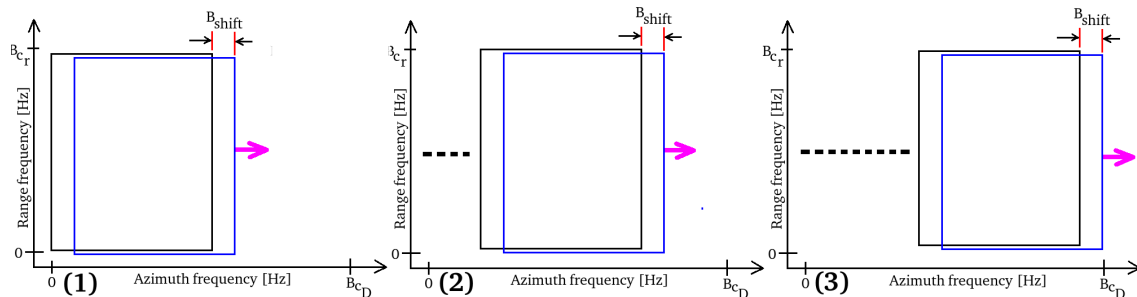


Figure 7. Doppler sub-aperture strategy. (1), (2), (3): Low, medium, high Doppler-frequency extrapolation respectively.

The explanation of the chirp-Doppler sub-aperture strategy, represented in Figure 7, is the following: We consider Figure 7, where master and slave sub-bands are generated by focusing the SAR image, where the matched filter is set to exploit a range-azimuth bandwidth equal to $B_{c_r}, B_{c_D} - B_{D_L}$. The not-processed bandwidths B_{D_L} are divided into N_D equally distributed bandwidths steps, respectively. At this point, N_c rigid shifts of the master-slave system are made along the azimuth bandwidth domain; this is made to

populate the entire row of (4) and (5). The process is repeated N_D times for each shift in azimuth; in fact, Figure 7(1–3) represent the azimuth frequency variation strategy when the Doppler bandwidth is located at N_D . At each Doppler frequency shift $\frac{B_{c_D} - B_{D_L}}{N_D}$, every element of (4) and (5) is populated.

3.2. Doppler Sub-Aperture Strategy

The decomposition of the SAR data into Doppler sub-apertures is formalized in this subsection, which is performed starting from the spectral representation of the focused SAR data. To this end, notice that the generic i -th chirp sub-aperture two-dimensional DFT of (2) is given by:

$$\begin{aligned} S_{SLC_{f_i}}(n, q) &= DFT2 \left\{ 2N\tau \exp \left[-j \frac{4\pi r}{\lambda} \right] \text{sinc} \left[\pi B_{c_{r_i}} (k - L_{c_g}) \right] \text{sinc} \left[\pi B_{c_D} (x - L_{D_h}) \right] \right\} \\ &= 2N\tau \exp \left[-j \frac{4\pi r}{\lambda} \right] \sum_{k=0}^{N-1} \sum_{x=0}^{M-1} \text{sinc} \left[\pi B_{c_{r_i}} (n - L_{c_g}) \right] \text{sinc} \left[\pi B_{c_D} (q - L_{D_h}) \right] \\ &\quad \exp \left(-j \frac{2\pi kn}{N} \right) \exp \left(-j \frac{2\pi xq}{M} \right) \\ &= 2N\tau \exp \left[-j \frac{4\pi r}{\lambda} \right] \frac{1}{\pi B_{c_{r_i}}} \text{rect} \left[\frac{n}{\pi B_{c_{r_i}}} \right] \frac{1}{\pi B_{c_D}} \text{rect} \left[\frac{q}{\pi B_{c_D}} \right] \exp \left(-j 2\pi n L_{c_g} \right) \exp \left(-j 2\pi q L_{D_h} \right). \end{aligned} \quad (6)$$

From the last equation, it turns out that a single point stationary target has a two-dimensional rectangular nature with total length proportional to the range-azimuth bandwidths, respectively. The phase term $\exp(-j 2\pi n L_{c_g}) \exp(-j 2\pi q L_{D_h})$ is due to the sinc function dislocation in range and azimuth when the SLC SAR data are considered. In the SAR, the movement of a point target with velocity in both the range and azimuth direction is immediately warned by the focusing process, resulting in the following anomalies:

- Azimuth displacement in the presence of target constant range velocity;
- Azimuth smearing in the presence of target azimuth velocity or target range accelerations;
- Range-walking phenomenon, visible as range defocusing, in the presence of target range speed; backscattered energy can be detected over one or more range resolution cells.

According to (6), it turns out that a single point stationary target has a two-dimensional rectangular nature with total length proportional to the range-azimuth bandwidths respectively. The phase term $\exp(-j 2\pi n L_{c_g}) \exp(-j 2\pi q L_{D_h})$ is due to the sinc function dislocation in range and azimuth when the SLC SAR data are considered. In the SAR, the movement of a point target with velocity in both range and azimuth direction is immediately warned by the focusing process, resulting in the following anomalies:

- azimuth displacement in the presence of target constant range velocity;
- azimuth smearing in the presence of target azimuth velocity or target range accelerations;
- range-walking phenomenon, visible as range defocusing, in the presence of target range speed, backscattered energy can be detected over one or more range resolution cells.

In real cases, the backscattered energy from moving targets is distributed over several range-azimuth resolution cells. As a matter of fact, considering the point-like target T_1 (of Figure 3a) that is moving at \vec{v}_t whose (slant-range)-azimuth and acceleration components are $\{v_{rs}, v_a\}$, and $\{a_r, a_a\}$, respectively, then we can write

$$\begin{aligned} R^2(t) &= (Vt - S_a)^2 + (R_0 - S_r)^2 \text{ with } S_r = v_{r_s}t + \frac{1}{2}a_r t^2 \text{ and } S_a = v_a t + \frac{1}{2}a_a t^2 \\ |R(t)| &= |R_0 - S_r| \left\{ 1 + \frac{(Vt - S_a)^2}{(R_0 - S_r)^2} \right\}^{\frac{1}{2}}. \end{aligned} \quad (7)$$

We consider the following Taylor expansion:

$$(1+x)^\beta \approx 1 + \beta x \quad (8)$$

and that $R_0 - S_r \approx R_0$, and $(Vt - S_a)^2 \approx V^2 t^2 - 2VtS_a$, (7) can be written in the following form:

$$\begin{aligned} |R(t)| &= \left\{ |R_0 - S_r| + \frac{1}{2} \frac{(Vt - S_a)^2}{(R_0 - S_r)} \right\} = |R_0 - S_r| + \frac{V^2 t^2}{2R_0} \left(1 - \frac{2S_a}{Vt} \right) \\ &= R_0 - S_r + \frac{V^2 t^2}{2R_0} - \frac{Vt S_a}{R_0} \\ &= R_0 - v_{r_s} t - \frac{1}{2} a_r t^2 + \frac{V^2 t^2}{2R_0} - \frac{Vt \left(v_a t + \frac{1}{2} a_a t^2 \right)}{R_0} \\ &= R_0 - v_{r_s} t - \frac{1}{2} a_r t^2 + \frac{V^2 t^2}{2R_0} - \frac{Vv_a t^2}{R_0} - \frac{Va_a t^3}{2R_0}. \end{aligned} \quad (10)$$

Neglecting $\frac{Va_a t^3}{2R_0}$ and approximating $(V^2 - 2Vv_a) \approx (V - v_a)^2$, Equation (10) can be written like:

$$|R(Vt)| = R_0 - v_{r_s} t + \frac{t^2}{2R_0} [(V - v_a)^2 - R_0 a_r], \quad (11)$$

recasting (11) in terms of $x = Vt$, we obtain [65]:

$$|R(x)| = R_0 - \epsilon_{r_1} x + \left[(1 - \epsilon_{c_1})^2 - \epsilon_{r_2} \right] \frac{x^2}{2R_0}, \quad x = Vt, \quad (12)$$

where:

- $\epsilon_{r_1} = \frac{v_{r_s}}{V}$ (due to range velocity);
- $\epsilon_{r_2} = \frac{a_r R_0}{V^2}$ (due to range acceleration);
- $\epsilon_{c_1} = \frac{v_c}{V}$ (due to azimuth velocity).

The above presented terms, as shown in [65], modify the received signal, and should be taken into account in Equation (6).

4. Tomographic Model

Considering a single SLC image from which we applied the MCA according to the frequency allocation strategy depicted in Figure 7, the tomogram represented by the line of contiguous pixels shown in Figure 8 is calculated. The vibrations present on the tomographic plane extending from the Earth's surface to a depth of a few kilometers is assessed. The figure represents a series of harmonic oscillators anchored on each pixel of the tomographic line, which is symbolically represented as a spring linked to a mass and oscillating due to the application of harmonic vibrations. Each wave generated by each harmonic oscillator bounces off the surface of the Earth, as there is an abrupt variation in the density of the medium (the ground-air boundary). On each pixel, a vibrational phasor is observed in time applying Doppler MCA [52,54]. Through the orbital change of view

(which is performed in azimuth), an effective subsurface in-depth vibrational scan of the Earth is achieved.

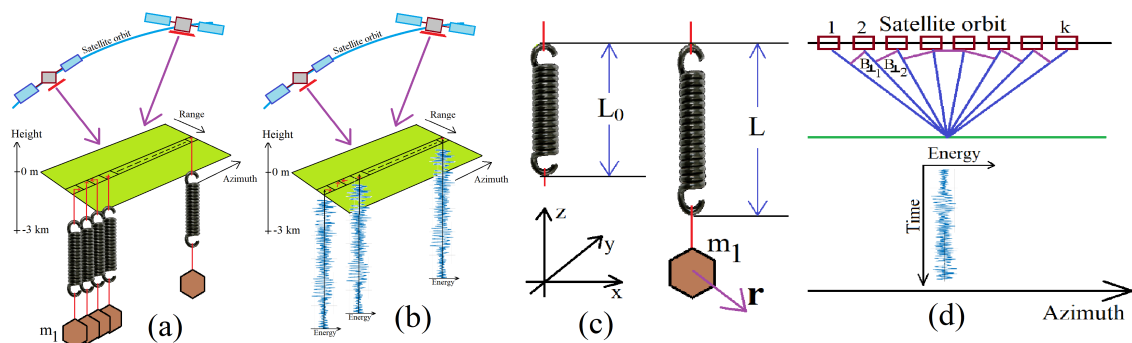


Figure 8. Tomographic acquisition geometry. (a): SAR acquisition of targets represented by harmonic mass oscillators. (b): SAR acquisition of targets represented by time-domain harmonic vibration functions. (c): Static representation in a 3D spatial reference system of a spring when expanded by a mass. The spring from a length L_0 is diluted by gravity acting on the mass m_1 , to a length L . (d): Details of the tomographic acquisition geometry along the satellite orbit. All orthogonal baselines are represented.

Vibrational Model of the Earth

The proposed vibrational model of the Earth surface is schematically shown in Figure 8a,b. The geometrical reference system for both sub-pictures is the range, azimuth and altitude three-dimensional space. For the present case, the vertical dimension represents the depth below the topographic level (for this specific case, the medium boundary is represented by the green plane). The tomographic line of interest is constituted of the series of contiguous pixels laying on the green plane. As can be seen from Figure 8a, on each pixel belonging to the tomographic line, a mass is hanging using a spring. This system is now induced to oscillate harmonically due to the seismic background ripple, the city of Cairo human activities and the wind force field. These oscillations are schematized as the vibration energy function visible in Figure 8b. In this context, the radar instantaneously perceives this coherent harmonic oscillation. From a mathematical point of view, the Earth displacement is perceived as a complex shift belonging on each pixel of interest. Each instantaneous displacement is estimated between the master image with respect to the slave, where the shifts are estimated through the pixel tracking technique [52,54]. The computational flowchart in Figure 9 schematically describes the computational flow from a single SAR image to a tomographic estimate. Computational block 1 represents the single SAR image in the SLC configuration. Computational blocks 2 and 3 are bandpass filters and operate according to the frequency allocation strategy in Figure 7. These filters play a crucial role in the estimation of displacements that are equal to vibration. Computational block 4 represents a spatial filter that only performs vibration estimation on the points representing the tomographic line under consideration. Computational block 5 implements the vibration metric algorithm, and finally, computational block 6 performs the focusing of the estimated acoustic waves in order to obtain the internal tomography of the distributed target crossed by the tomographic line.

The number of tomographic independent looks (depending on the total number of Doppler sub-apertures) is defined by the parameter k .

We suppose now the spring is being perturbed by an impulsive force. According to this perturbation, the rope begins to vibrate, describing a harmonic motion (in this context, we are not considering any form of friction). The resulting perturbation moves the rope through the space-time in the form of a sinusoidal function. The seismic wave will then reach a constraint end that will cause it to reflect in the opposite direction. The reflected wave will then reach the opposite constraint that will make it reflect in the original direction and return in the initial location, maintaining the same frequency and amplitude. According

to Classical Physics principles, the rebounding wave is superimposed on the arriving wave, and the interference of two sine waves with the same amplitude and frequency propagating in opposite directions leads to the generation of an ideal and perpetual standing wave on the spring. Each vibrational channel is now considered when the spring is able to oscillate into the three-dimensional space, according to specific perturbation nature. When the Earth vibrates, it happens that the length of the spring must also fluctuate. This phenomenon causes oscillations in the tension domain of the spring. It is clear that these oscillations (i.e., the longitudinal ones) propagate through a frequency approximately twice as high as the frequency value of the transverse vibrations. The coupling between the transverse and longitudinal oscillations of the spring can essentially be modeled through non-linear phenomena.

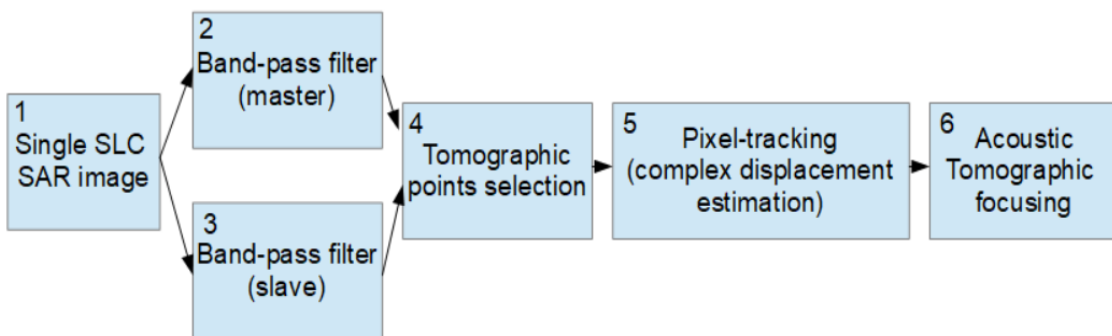


Figure 9. Computational flowchart for estimating the internal results.

Figure 8c,d illustrates the oscillating model in the Euclidean space–time coordinates (x,y,z,t) , where the satellite motion has been purified from any orbital distortions, so that the geometric parameters used to perform the tomographic focusing can be rigorously understood. From Figure 8c, L is the length of the spring when it is at its maximum tension, while L_0 is its length when no mass is present. Finally, the spring has been considered to have an elastic constant equal to ξ . The vibrational force applied to the mass m_1 of Figure 8c is equal to [68]:

$$F = -4\xi \mathbf{r} \left(1 - \frac{L_0}{\sqrt{L^2 + 4\mathbf{r}^2}} \right). \quad (13)$$

If $\mathbf{r} \ll L$, (13) is expanded in the following series:

$$F = -4\xi \mathbf{r}(L - L_0) \left(\frac{\mathbf{r}}{L} \right) - 8\xi L_0 \left[\left(\frac{\mathbf{r}}{L} \right)^3 - \left(\frac{\mathbf{r}}{L} \right)^5 + \dots \right], \quad (14)$$

where a precise approximation of (14) is the following cubic restoring force:

$$F = m\ddot{\mathbf{r}} \approx -4\xi \mathbf{r}(L - L_0) \left(\frac{\mathbf{r}}{L} \right) \left[1 + \frac{2L_0}{(L - L_0)} \left(\frac{\mathbf{r}}{L} \right)^2 \right]. \quad (15)$$

where the non-linearity condition dominates when $L \approx L_0$. If we define:

$$\omega_0 = \frac{4\xi}{m} \left[\frac{(L - L_0)}{L} \right], \quad (16)$$

and

$$\xi = \frac{2L_0}{L^2}(L - L_0), \quad (17)$$

and taking into account (15) we have:

$$\ddot{\mathbf{r}} + \omega^2 \mathbf{r} (1 + \xi \mathbf{r}^2) = 0. \quad (18)$$

When considering damping and forcing, (18) is modified as:

$$\ddot{\mathbf{r}} + \lambda \dot{\mathbf{r}} + \omega^2 (1 + \xi \mathbf{r}^2) \mathbf{r} = \mathbf{f}(\omega t), \quad (19)$$

where $\mathbf{f}(\omega t)$ is the forcing term and λ is the damping coefficient. If non-linearity of (19) is sufficiently low, it can be reduced into the following two-degree-of-freedom linear harmonic oscillator:

$$\mathbf{r}(t) = (a \cos \omega_0 t, b \sin \omega_0 t) \exp\left(\frac{-\lambda t}{2}\right) \quad (20)$$

where $\{a, b\}$ are the instantaneous shifts estimated by the coregistrator. The harmonic oscillator (20) contains the displacement parameters $\epsilon_{r_1}, \epsilon_{r_2}, \epsilon_{c_1}$ estimated by (12). According to Figure 8d the vector representation of k samples of the time-domain function (20) consisting in the following multi-frequency data input is considered:

$$\mathbf{Y} = [\mathbf{y}(1), \dots, \mathbf{y}(k)], \in \mathbf{C}^{k \times 1}. \quad (21)$$

We introduce here the sonic steering matrix $\mathbf{A}(z) = [\mathbf{a}(z_{min}), \dots, \mathbf{a}(z_{MAX})], \in \mathbf{C}^{k \times F}$ contains the phase information of to the Doppler frequency variation of the sub-aperture strategy, associated to a source located at the elevation position $\mathbf{z} \in \{z_{min}, z_{MAX}\}$,

$$\mathbf{A}(\mathbf{K}_z, \mathbf{z}) = \begin{bmatrix} 1, \exp(j2\pi k_{z_2} t z_0), \dots, \exp(j2\pi k_{z_{k-1}} t z_0) \\ 1, \exp(j2\pi k_{z_2} t z_1), \dots, \exp(j2\pi k_{z_{k-1}} t z_1) \\ \dots \\ 1, \exp(j2\pi k_{z_2} t z_{F-1}), \dots, \exp(j2\pi k_{z_{k-1}} t z_{F-1}) \end{bmatrix}, \quad (22)$$

where $\mathbf{K}_z = \frac{4\pi B_\perp}{\lambda r_i \sin \theta}, i = 1, \dots, k$, B_\perp is the i -th orthogonal baseline which is visible in Figure 8d, and r_i is the i -th slant-range distance. The standard sonic tomographic model is given by the following relation:

$$\mathbf{Y} = \mathbf{A}(\mathbf{K}_z, \mathbf{z}) \mathbf{h}(\mathbf{z}), \quad (23)$$

where in (23), $\mathbf{h}(\mathbf{z}) \in \mathbf{C}^{1 \times F}$, inverting (23), I finally find the following tomographic solution:

$$\mathbf{h}(\mathbf{z}) = \mathbf{A}(\mathbf{K}_z, \mathbf{z})^\dagger \mathbf{Y}. \quad (24)$$

In (24), the steering matrix $\mathbf{A}(\mathbf{K}_z, \mathbf{z})$ represents the best approximation of a matrix operator performing the digital Fourier transform (DFT) of \mathbf{Y} . The tomographic image $\mathbf{h}(\mathbf{z})$, which represents the spectrum of $\mathbf{A}(\mathbf{K}_z, \mathbf{z})$, is obtained by doing pulse compression.

The tomographic resolution is equal to $\delta_T = \frac{\lambda R}{2A}$, where λ is the sound wavelength over the Earth, R is the slant range, and A is the orbit aperture considered in the tomographic synthesis; in other words, it consists of the Doppler bandwidth used to synthesize the sub-apertures. The maximum tomographic resolution obtainable using these SLC data, synthesized at 24 kHz, is as follows. Considering an average speed of propagation of the seismic waves of about $v \approx 6000$ m/s, a frequency of investigation set by us equal to 12,500 Hz, the wavelength of these vibrations is equal to about $\lambda = \frac{v}{f} \approx \frac{6000}{24,000} \approx 0.24$ m. Considering the above parameters, extending the tomography to the maximum orbital aperture equal to half the total length of the orbit, therefore about 42,000 m, with $R = 650,000$ m, the tomographic resolution is equal to $\delta_z = \frac{\lambda R}{2A} = \frac{0.24 \cdot 650,000}{2 \cdot 42,000} \approx 0.92$ m. This is the tomographic resolution set to calculate all the experimental parts shown in Section 5.

5. Experimental Results

In this section, we will show all the experimental results that have been made and have been divided into external, and internal, experimental results. In the first case, we show the results provided by SAR interferometry (InSAR). These consist of the evaluation of radar interferometric fringes to demonstrate the actual shapes of the outer facades of all pyramids in the Giza Plateau. The detailed explanation is provided in Section 5.1. Similarly, the results for the internal vibrational tomography analysis of Khnum-Khufu alone are discussed in detail in Section 5.2.

5.1. External Experimental Results

This subsection shows and discusses all the results obtained with the aim of revealing new features of the external appearance of all pyramids residing on the Giza Plateau. In order to achieve this goal, we employed the InSAR technique and evaluated the nature of the interferometric fringes and discovered, through the measurement of their inclination, that all pyramids do not each consist of four faces but of eight faces. We processed data according to the images listed in Table 2, from picture 1 to 6. We found that each face of each pyramid had an inwards bow that became more relevant closer to the ground much like a trough. Figure 10 shows the interferometric fringes generated by two SAR repeat-pass acquisitions with a suitable spatial baseline in order to generate a series of well-estimated interferometric fringes imprinted on the faces of the pyramids. The interferometric acquisition was performed along a time baseline equal to the complete orbital cycle of the single COSMO-SkyMed Second Generation (CSG) satellite, which coincides with 16 days. In spite of the substantial number of waiting days, the interferometric acquisition appears not to be very noisy, and this quality is confirmed through the evaluation of the coherence parameter whose map is represented in Figure 11. This result appears very good, as a large part of the figure, removing all the areas where the radar shadow is present, and it maintains coherence levels very close to 1.

Table 2. List of processed COSMO-Sky-Med SAR images.

Picture	Date	Orbit	Beam	Polarization	Experiment
1	28 October 2021	Right-descending	06 (master)	HH	External
2	13 November 2021	Right-descending	06 (slave)	HH	External
3	27 October 2021	Right-descending	08 (master)	HH	External
4	12 November 2021	Right-descending	08 (slave)	HH	External
5	24 July 2021	Right-ascending	39 (master)	HH	External
6	9 August 2021	Right-ascending	39 (slave)	HH	External
7	25 February 2022	Left-descending	46 (single image)	VV	Internal
8	16 November 2021	Right-descending	48 (single image)	HH	Internal
9	22 February 2022	Right-descending	48 (single image)	VV	Internal
10	16 February 2022	Right-ascending	48 (single image)	VV	Internal
11	25 March 2022	Right-descending	48 (single image)	VV	Internal
12	26 April 2022	Right-descending	48 (single image)	VV	Internal

Figure 12a represents the details of the InSAR fringes measured on the three pyramids (Khufu, Kefren, and Menkaure), while Figure 12b shows the detail of the pyramid of Khnum-Khufu, and finally, Figure 12c is the pyramid of Kefren. Figure 13a–d show the particular representations of the SAR interferometric fringes observed on the east face of the Pyramid of Khnum-Khufu (in box (a)). The remaining boxes (b), (c) and (d), represent the first, second and third interferometric fringes observed on the north face of the same pyramid, starting from the bottom. The inclination of the entire face of the pyramid is clearly observed, having symmetry along the height of the geometric figure. The north face of the Khnum-Khufu pyramid is depicted in Figure 14a, while the details of the first, second and third fringe (starting from the ground plane) are shown in Figure 14b–d, respectively. Here again, the same effect is observed whereby the single face is divided into two indented

half-faces. The west face also presents the same architectural feature; in fact, Figure 15a depicts the extension of the interferometric fringes extended over the entire south face, while the details of the first, second and third fringes (always starting from the ground plane) are shown in Figure 15b–d, respectively.

We now move to the pyramid of Kefren to repeat the same experiments where the same qualitative evaluation of the SAR interferometric fringes present on the three facets of it, except for the south one, will be carried out, reaching the identical conclusions made for the pyramid of Khufu. Figure 16a–d shows the particular representation of the SAR interferometric fringes observed on the west face of the Pyramid of Kefren (in box (a)). The remaining boxes (b), (c) and (d), represent the first, second and third interferometric fringes observed on the north face of the same pyramid, starting from the bottom. The north front of the second Kefren pyramid is analyzed in Figure 17a, depicting the extent of the interferometric fringes as a whole, while the details of the first, second and third fringes (starting from the ground plane) are shown in Figure 17b–d, respectively. The south façade is also studied in Figure 18a, along with its first, second and third fringe details (starting from the ground plane), which are shown in Figure 18b–d, respectively.

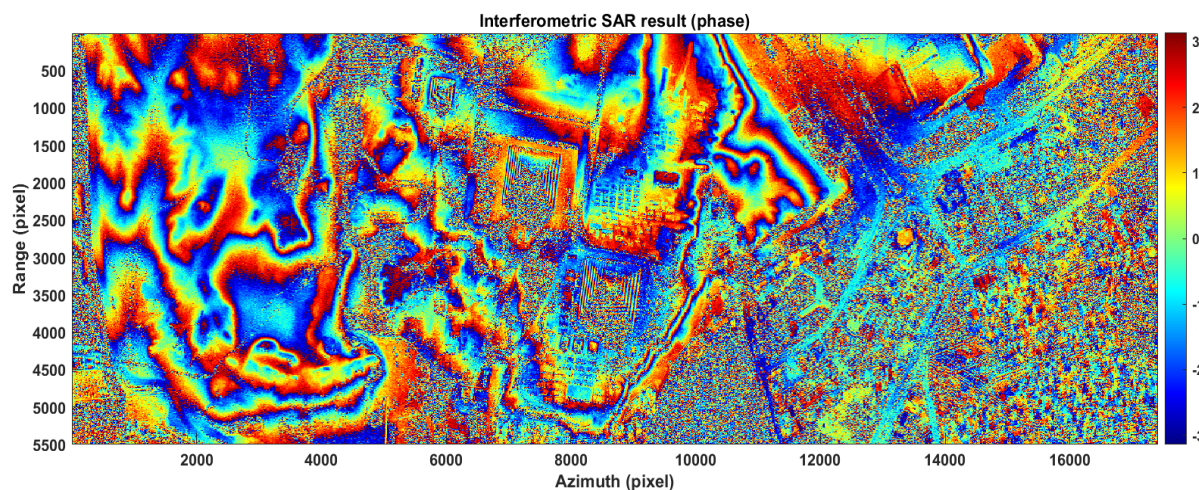


Figure 10. SAR image representing the interferometric repeat-pass phase of the Giza plateau.

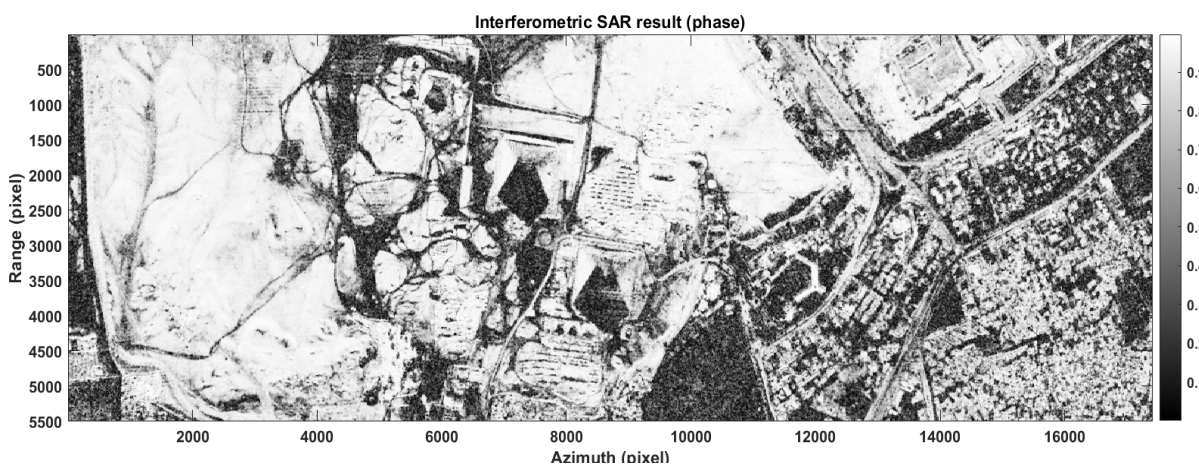


Figure 11. SAR image representing the interferometric repeat-pass coherence of the Giza plateau.

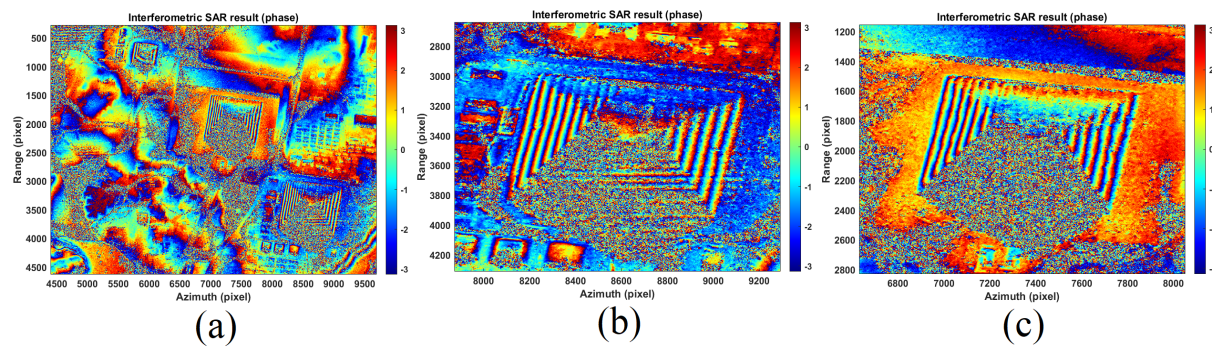


Figure 12. Interferometric SAR results. (a): Interferometric fringes of the Giza plateau. (b): Interferometric fringes of Khnum-Khufu. (c): Interferometric fringes of Khefren.

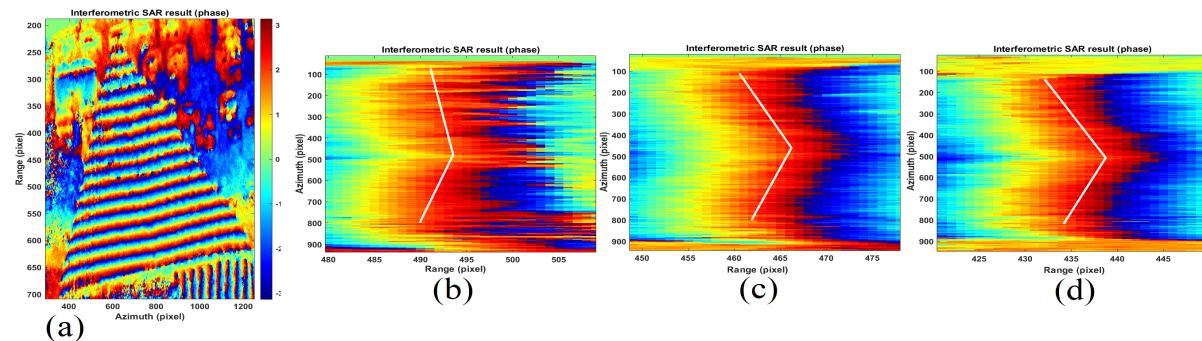


Figure 13. Representation in particular of the pyramid of Khnum-Khufu. Interferometric phases. (a): east side. (b–d): magnification of interferometric fringe 1, 2, and 3.

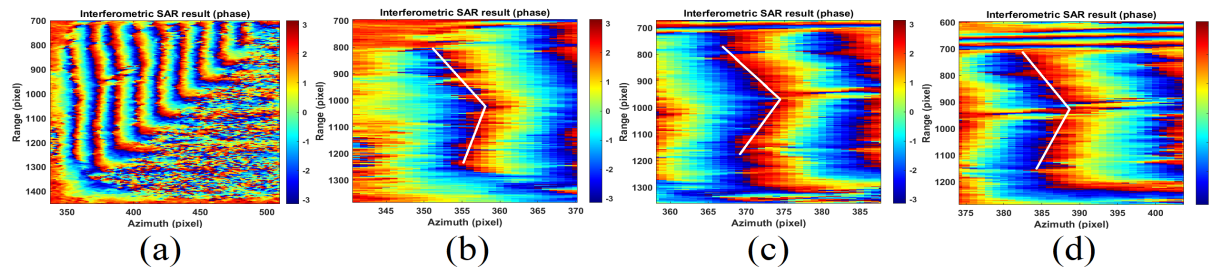


Figure 14. Representation in particular of the pyramid of Khnum-Khufu. Interferometric phases. (a): north side. (b–d): magnification of interferometric fringe 1, 2, and 3.

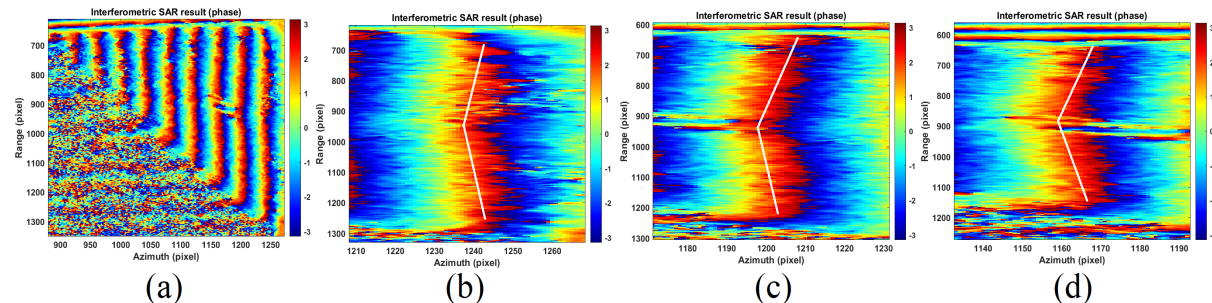


Figure 15. Representation in particular of the pyramid of Khnum-Khufu. Interferometric phases. (a): south side. (b–d): magnification of interferometric fringe 1, 2, and 3.

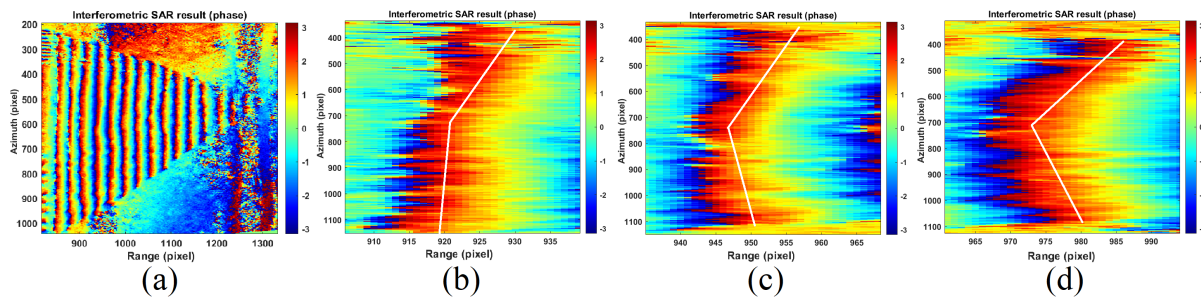


Figure 16. Representation in particular of the pyramid of Kefren. Interferometric phases. (a): west side. (b–d): magnification of interferometric fringe 1, 2, and 3.

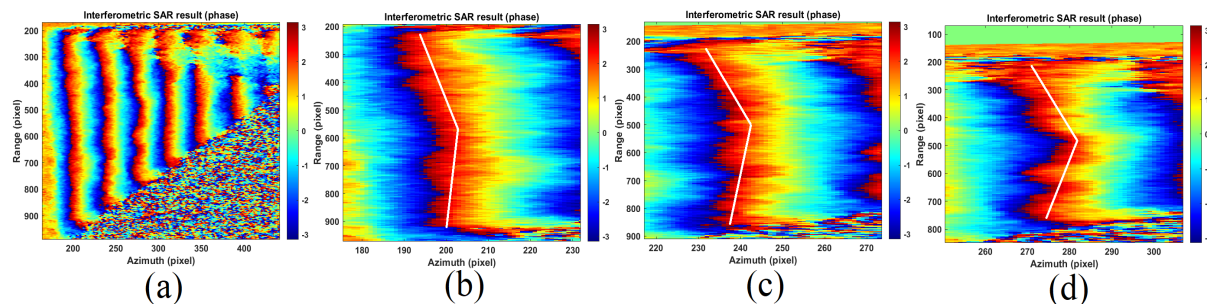


Figure 17. Representation in particular of the pyramid of Kefren. Interferometric phases. (a): north side. (b–d): magnification of interferometric fringe 1, 2, and 3.

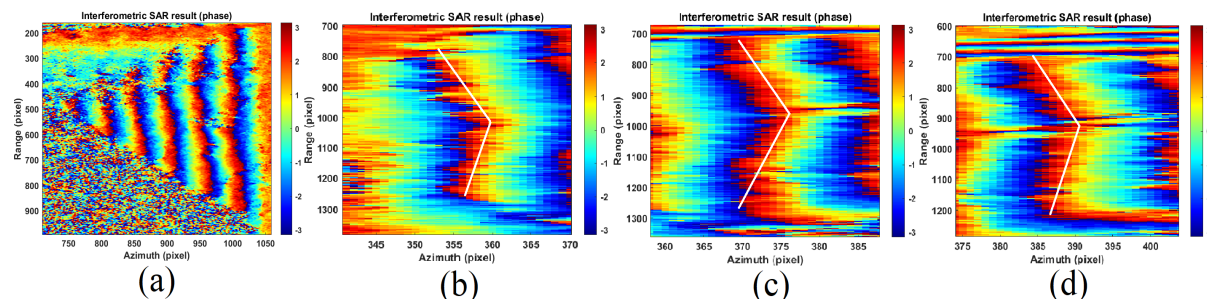


Figure 18. Representation in particular of the pyramid of Kefren. Interferometric phases. (a): south side. (b–d): magnification of interferometric fringe 1, 2, and 3.

Although much smaller, the pyramid of Menkaure is also well represented by the interferometric radar. As a matter of fact, Figure 19a–d depict the entire pyramid (in Figure 19a), while Figure 19b–d depict the first fringe starting from the ground plane of the east, west, and north faces, respectively. Surprisingly, the pyramid of Menkaure also consists of eight facets and not four (while maintaining the fact that the south face could not be observed because it was in radar shadow). This subsection, which focused on presenting the results of external measurements alone, ends by rigorously demonstrating, through radar measurements, the eight-sided nature of the three pyramids of Khufu, Kefren and Menkaure. In the next subsection, the internal measurements that were made from space will be detailed in order to carry out for the first time the complete internal mapping of all structures belonging to the pyramid of Khnum-Khufu alone. In order to ensure the reliability of the data, we show the correspondence of the displacement of the anomaly trend on the west face only, where we compared the data measured by the radar with those generated by the Lidar. Here, we show the plots of both profiles with relative errors. In Figure 20a, we show the displacement trend of the interferometric fringe in Figure 16c. The unfiltered trend is represented by the blue function, while the filtered trend is represented by the black trajectory. Figure 20b instead shows the trend of the measurements, taken along the same trajectory travelled by the interferometric fringes,

but in this case generated by the Lidar. Again, the unfiltered trend is represented by the blue function, while the filtered trend is represented by the black trajectory. Figure 20c shows the superposition of SAR and Lidar measurements, confirming the same trend. In fact, Figure 21a shows the superposition of the filtered functions of both SAR and Lidar, and Figure 21b quantifies the error existing between the two. Again, the blue-colored function is the unfiltered one, while the black one represents the filtered. As can be seen from the trend, the error is very low: it is quantifiable at about 0.1 meters at its maximum value of about 35 cm.

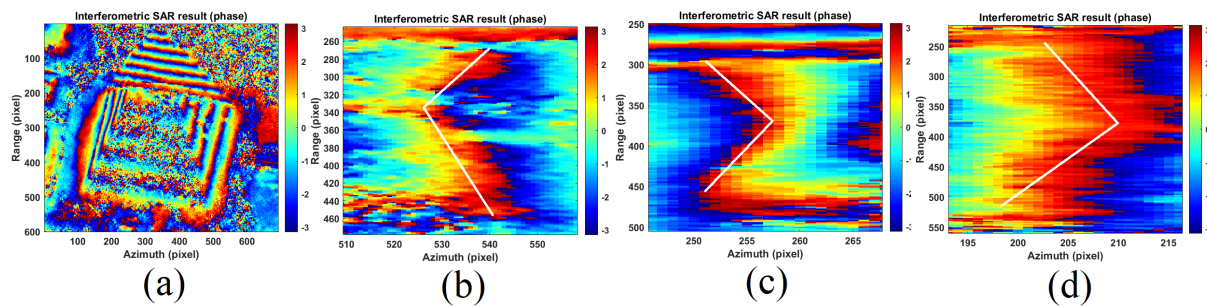


Figure 19. Representation in particular of the pyramid of Menkaure. Interferometric phases. (a): Menkaure pyramid. (b): east side interferometric fringe particular. (c): west side interferometric fringe particular. (d): north side interferometric fringe particular.

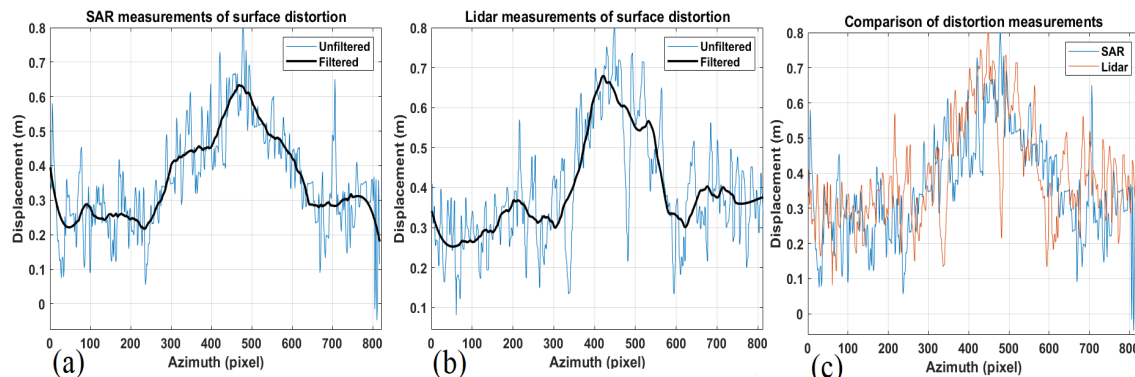


Figure 20. Displacement measurements. (a): SAR displacement. (b): Lidar displacement. For (a,b), the blue functions are the unfiltered trends, while the black plot are filtered. (c): Comparison of SAR versus Lidar displacement measurements.

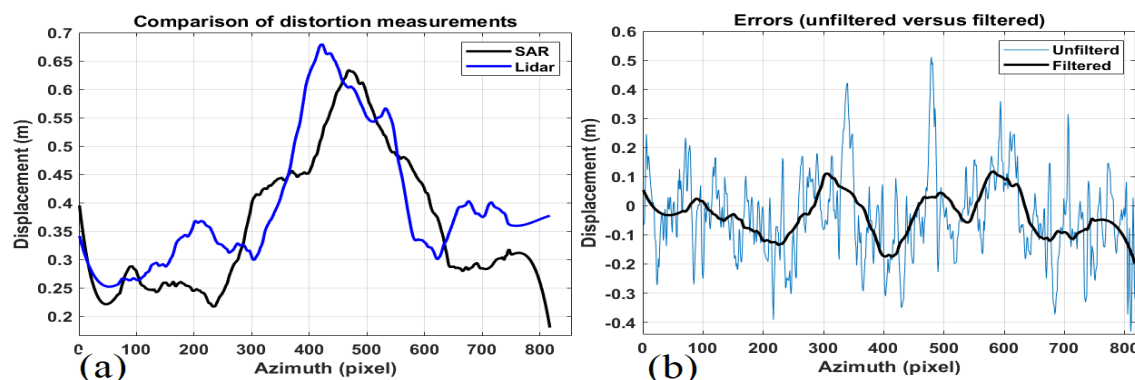


Figure 21. (a): Filtered displacement measurements. (b): Errors between SAR and Lidar displacement trends.

5.2. Internal Experimental Results of Khnum-Khufu

Data analysis obtained using the SAR tomographic Doppler imaging technique was able to provide clear objective elements to understand the internal structure of the pyramid

of Khnum-Khufu. When proposing our results, we start by describing the well-known structures and then move on to the description of some of the unknown structures. The internal imaging obtained from multiple angles allows us to obtain an accurate 3D model that gave us the possibility, like never before, of taking a look inside one of the most important and mysterious megalithic monuments in the world. We processed data according to the images listed in Table 2, from pictures 7 to 12. In the calculation of the internal experimental results, we have not taken into account the effects due to multiple reflections (multipath) of the sound wave. In fact, as this research is in its current state, we will also try to take these interference effects into account in the near future, as they could negatively perturb the tomographic measurement. One fundamental thing, however, has been to greatly attenuate disturbances due to both radar electromagnetic multipath and disturbances due to SAR layover and foreshortening. To achieve this, we made sure to appropriately choose the tomographic lines investigating the pixels where the radar image was pure, i.e., where the considered resolution cell was produced by the contribution of a single scattering effect, and not by the sum of several effects, due to the particular slant projection geometry and the plane wave approximation. In order to obtain the best metric interpretation of the tomographic experimental results, it is necessary to consider that the horizontal axis of each tomogram is that of the tomographic lines and follows the resolution of the radar, while the vertical axis is estimated through the sound focusing algorithm and therefore is applied by algorithm (24). In this context, it is possible to state without any reasonable doubt that each pixel corresponds to 1 m of spatial resolution in space.

This subsection describes all the tomographic measurements, and the entire internal architecture of Khnum-Khufu has been redesigned, which we propose in Figure 22. The complete list of rooms, corridors and tunnels that had never been inventoried until now is shown in Table 3. Each structure (simple or complex) was assigned to a unique tag numbered from 1 to 20, according to Figure 22. For this work, we have not used any kind of simulated data or predictive mathematical model, but rather, we report in a scientific manner what the CSG satellite has brought to our attention. Here, we list the explanation of all the results obtained respecting the order given in Table 3. Each structure listed in Table 3 will be described in detail, identified in the tomography and reconstructed within a Computer-Aided Design and Drafting (CAD) environment where all measurements will be provided. For the sake of clarity, we have included Table 4 that has the task of connecting each structure, tagged with a unique number increasing from 1 to 20, through its description, to the tomographic figure on which it is detected.

Table 3. List of discovered structures.

Structure Number	Structure Type	Structure Name
1	Corridor	Eastern ascending ramp
2	Corridor	Western ascending ramp
3	Corridor	Southern corridor
4	Corridor	Eastern descending ramp
5	Corridor	Western descending ramp
6	Corridor	Northern underground corridor
7	Corridor	Northern–East underground corridor
8	Corridor	Northern–West underground corridor
9	Complex structure	Northern underground complex structure
10	Complex structure	Zed complex structure
11	Room	Eastern sarcophagus passage facility
12	Room	Western sarcophagus passage facility
13	Room	Bottom sarcophagus room facility
14	Room	Queen’s bottom room
15	Room	Southern bottom room
16	Corridor	Southern connection
17	Room	Little void
18	Corridor	Front corridor
19	Room	Big void
20	Complex structure	Zed–big void double connection

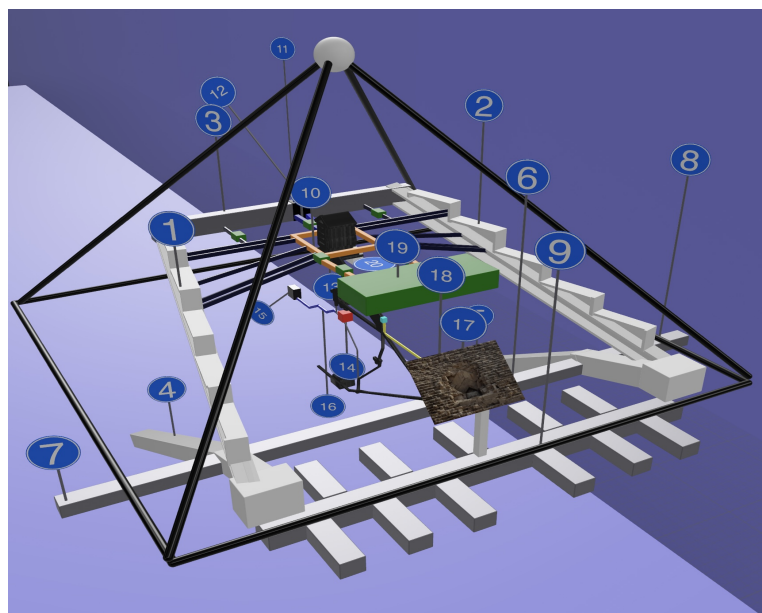


Figure 22. Three-dimensional (3D) reconstruction of the pyramid of Khnum-Khufu downstream of the interpretation of tomograms estimated through radar ultrasound.

5.3. Imaging of Known Structures

Before describing what has been discovered (what is still unknown), we propose the imaging of the known objects, in particular the King's room, the Zed, the Queen's room, the Grand Gallery, the grotto, and the so-called unfinished room. The SAR image of the pyramid is shown in Figure 23a, while the internal diagram of the pyramid, oriented toward the north (the northern direction goes from left to right) is shown in Figure 23b. The first tomographic result is presented in Figure 24a,b. This result is illustrated in Figure 23a by means of two yellow lines (identified by the number 1) that extend from the ground toward the pyramid apex. By estimating the vibrations, the pyramid is transparent due to their penetration characteristics within the solid rock, and its internal structures can be observed in Figure 24a,b. Figure 24a represents the sonic tomography partially overlapped with the picture in Figure 23b, while Figure 24b shows the non-overlapped tomography where three areas of interest are shown, and the details are studied below. Figure 25a–c is the detailed representation of the Zed, located inside box number 1 of Figure 24b, where Figure 25a is the schematic representation, while Figure 25b,c are the partially overlapped and not-overlapped tomography magnitude images, respectively. The Queen's chamber particular is depicted in Figure 26a–c; here, we use the same representation strategy where Figure 26a is the room scheme and Figure 26b,c are the partially overlapped and not-overlapped tomography, respectively. Figure 27a,b is the detailed image contained within the red box 3 of Figure 24b, and the void commonly referred to as 'the Grotto' is clearly visible. The lower chamber, the one commonly referred to as 'the unfinished room', is detected by radar, although with a weak signal, within the white box number 2. The Queen's room appears to be connected through a corridor connecting the grotto to the room below. This corridor, although it appears to be abruptly interrupted, is detected through a radar signature, which is marked by the white arrow number 3. It is assumed that this corridor follows the trajectory indicated by the red line, which is also pointed out by the white arrow number 3. Figure 2b,c show the detailed figure of the Zed, the colossal monument located at the heart of the pyramid (visible in Figure 24a). Figure 2b is its representation along the west–east direction, while Figure 2c shows its pattern along the south–north direction. Concluding this section, we propose in Figure 28a,b the partially and not-overlapped tomography of the Zed, respectively, where also the King's chamber is visible.

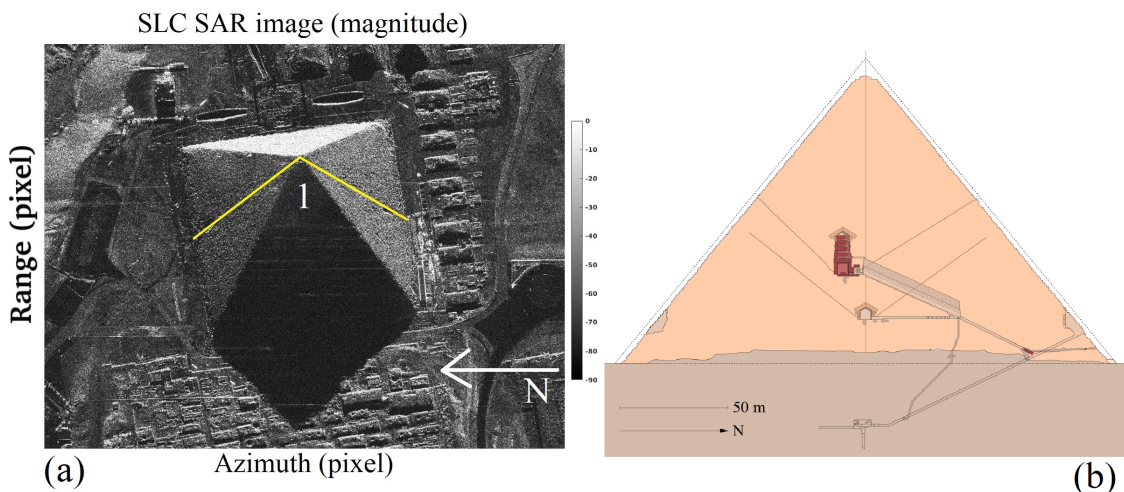


Figure 23. (a): SLC SAR of the pyramid of Khnum-Khufu. The V-shaped plot represents the tomographic line for which the vibrations were calculated, so that the inner section of the pyramid can be represented. (b): Internal scheme of the known structures.

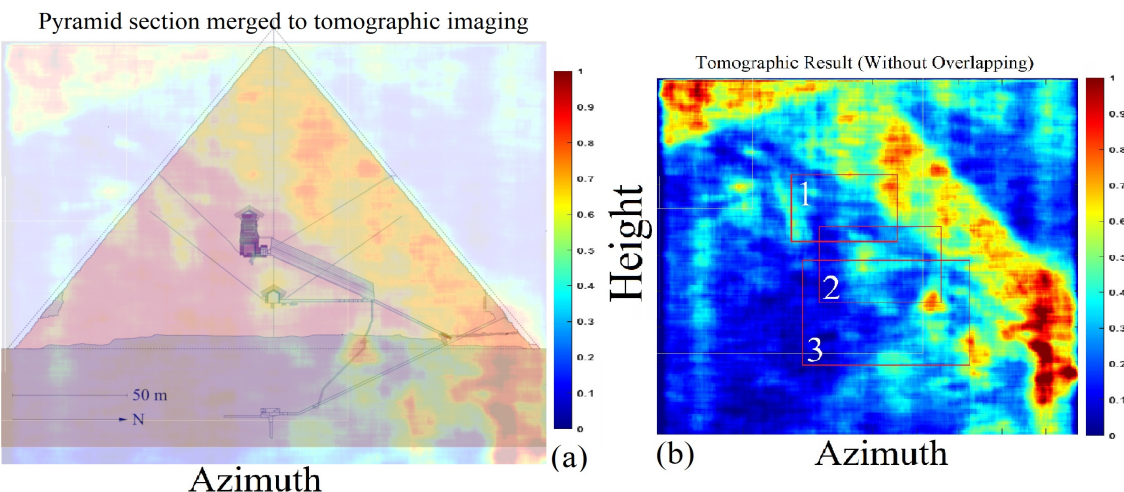


Figure 24. (a): Tomographic map of Khnum-Khufu overlapped to its schematic representation. (b): Tomographic map of Khnum-Khufu.

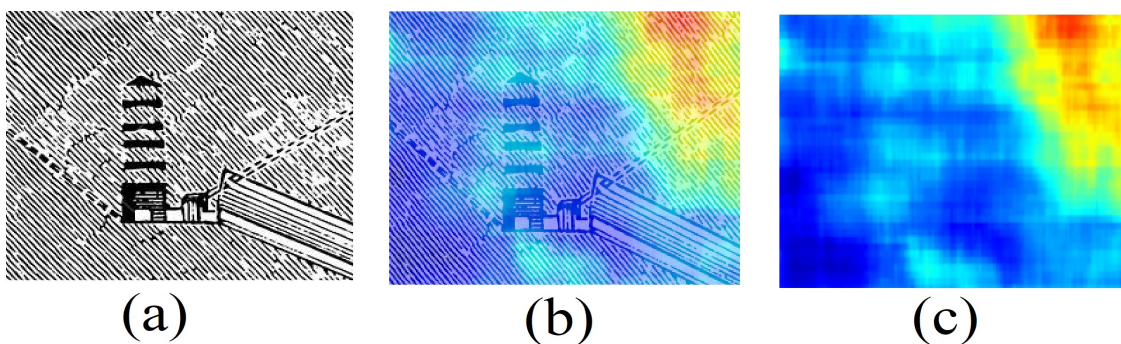


Figure 25. (a): Schematic representation of the Zed (box 1 details of Figure 24b). (b): Schematic representation of the Zed (box 1 details of Figure 24b) partially overlapped to tomographic result. (c): Figure 24b box 1 details tomographic result.